

RESEARCH ARTICLE

QUANTUM SIMULATION

String patterns in the doped Hubbard model

Christie S. Chiu¹, Geoffrey Ji¹, Annabelle Bohrdt^{2,1,3}, Muqing Xu¹, Michael Knap^{2,3}, Eugene Demler¹, Fabian Grusdt^{1,3}, Markus Greiner^{1*}, Daniel Greif¹

Understanding strongly correlated quantum many-body states is one of the most difficult challenges in modern physics. For example, there remain fundamental open questions on the phase diagram of the Hubbard model, which describes strongly correlated electrons in solids. In this work, we realize the Hubbard Hamiltonian and search for specific patterns within the individual images of many realizations of strongly correlated ultracold fermions in an optical lattice. Upon doping a cold-atom antiferromagnet, we find consistency with geometric strings, entities that may explain the relationship between hole motion and spin order, in both pattern-based and conventional observables. Our results demonstrate the potential for pattern recognition to provide key insights into cold-atom quantum many-body systems.

Quantum superposition describes quantum systems as simultaneously realizing different configurations. Such behavior is believed to be at the heart of phenomena in strongly correlated quantum many-body systems, which cannot be described by single-particle or mean-field theories. An intriguing consequence of the superposition principle is the existence of hidden order in correlated quantum systems: Although every individual configuration is characterized by a particular pattern, the average over these configurations leads to an apparent loss of order. By contrast, instantaneous projective measurements have the potential to reveal these underlying patterns.

One notable example of a system with hidden order is the one-dimensional (1D) Fermi-Hubbard model at strong coupling (*1*, *2*). Although 1D chains with additional holes or particles beyond an average of one particle per site (doped) yield average two-point spin correlations that decay more rapidly with distance than chains with an average of one particle per site (half-filled), this magnetic ordering can be revealed by accounting for the fluctuating positions across individual configurations of the additional dopants within each chain. The apparent loss of magnetic order is in fact hidden order, hidden by the dopants and their varying positions (*3*, *4*). Although direct detection of this hidden string order remains inaccessible in solids, experiments with ultracold atoms enable projective measurements, or “snap-

shots,” and generally can provide access to such structures (*5*). In particular, quantum gas microscopy (*6*) enables site-resolved imaging and access to correlators that have been constructed to reveal the hidden order (*7*).

The hidden order in 1D is well understood, but the physics of the 2D Hubbard model is fundamentally more complex because of an intricate interplay between spin and charge degrees of freedom; as a result, formulating an appropriate correlation function to search for hidden order becomes considerably more challenging. The 2D Hubbard model is believed to capture the rich physics of high-temperature superconductivity and other phases (*8–10*) such as the strange metal, stripe, antiferromagnet (AFM), or pseudogap phase, but a unified understanding of these phenomena is still lacking. For example, the behavior of individual dopants in an AFM is not agreed upon, including whether hidden string order is present and dopants hide magnetic correlations by shifting the positions of a string of spins. Quantum gas microscopy, however, provides a perspective that goes beyond the framework of two- or multipoint correlations. Hidden string order can be searched for directly within individual snapshots of the quantum mechanical wave function, where quantum fluctuations are resolved.

Here we perform a microscopic study of the hole-doped Fermi-Hubbard model and report indications of string patterns in 2D over a wide doping range. Our measurements use ultracold fermions in an optical lattice down to the lowest currently achievable temperatures, where at low doping AFM correlations extend across the system size (*11*). We identify string patterns in individual projective measurements and compare them with predictions from microscopic theoretical approaches.

Candidate theories for the doped Hubbard model

We study the Fermi-Hubbard model, which is defined by the Hamiltonian

$$\hat{H} = -t \sum_{\sigma=\uparrow,\downarrow} \sum_{\langle \mathbf{i}, \mathbf{j} \rangle} (\hat{c}_{\mathbf{i},\sigma}^\dagger \hat{c}_{\mathbf{j},\sigma} + \text{h.c.}) + U \sum_{\mathbf{j}} \hat{c}_{\mathbf{j},\uparrow}^\dagger \hat{c}_{\mathbf{j},\uparrow} \hat{c}_{\mathbf{j},\downarrow}^\dagger \hat{c}_{\mathbf{j},\downarrow} \quad (1)$$

(see Fig. 1A). The first term describes tunneling of amplitude *t* of spin- $\frac{1}{2}$ fermions $\hat{c}_{\mathbf{j},\sigma}$ with spin σ between adjacent sites \mathbf{i} and \mathbf{j} of a two-dimensional square lattice. The second term includes on-site interactions of strength *U* between fermions of opposite spin. We consider the strongly correlated regime, where $U \gg t$ and doubly occupied sites are energetically costly.

The Fermi-Hubbard model is well understood when the band is half-filled at an average of one particle per site (Fig. 1B). For temperatures $T \ll J$, where $J = 4t^2/U$ is the superexchange coupling, AFM correlations appear. Although these magnetic correlations are finite-ranged at nonzero temperatures, sufficiently cold finite-size systems can have AFM order across the entire system (*11*).

Much less is known about the doped Fermi-Hubbard model. However, it is understood that dopant delocalization for kinetic energy minimization competes with spin interactions in the background AFM. Experiments on the cuprates have also shown that at temperatures $T < J$ and between 10 and 20% doping, the pseudogap phase crosses over to the strange metal, located above the superconducting dome (*9*). These two metallic phases (pseudogap and strange metal) defy a description in terms of conventional quasiparticles and still lack a unified theoretical understanding.

Although phenomenological, numeric, and mean-field (MF) approaches have provided key insights in the past, quantum gas microscopy is naturally suited to assess microscopic theoretical approaches. One such theory is Anderson’s resonating valence bond (RVB) picture (*12*), which considers trial wave functions of free holes moving through a spin liquid composed of singlet coverings. We consider one particular class of RVB wave functions that have been studied extensively, called π -flux states (*13*). They stem from an MF density matrix $\hat{\rho} = \hat{P}_{\text{GW}} e^{-\hat{H}_{\text{MF}}/k_{\text{B}}T} \hat{P}_{\text{GW}}$, where k_{B} is Boltzmann’s constant, \hat{P}_{GW} is the Gutzwiller projection, and \hat{H}_{MF} is the quadratic Hamiltonian of itinerant fermions on a square lattice with a Peierls phase of π per plaquette [see section 6.1 of (*14*) for details]. Snapshots of the trial state in the Fock basis can be obtained by Monte-Carlo sampling, with temperature *T* as a free fit parameter (*15*).

A second microscopic approach that we examine is the geometric-string theory (*16*), where AFM order at half-filling is hidden in doped states via hole motion. This theory extends earlier work (*17–19*) and establishes a relationship between the AFM parent state at half-filling and the strongly correlated quantum states at finite doping. Here, holes move through the parent AFM by displacing

¹Department of Physics, Harvard University, 17 Oxford Street, Cambridge, MA 02138, USA. ²Department of Physics and Institute for Advanced Study, Technical University of Munich, 85748 Garching, Germany. ³Munich Center for Quantum Science and Technology (MCQST), Schellingstr. 4, D-80799 München, Germany.

*Corresponding author. Email: greiner@physics.harvard.edu

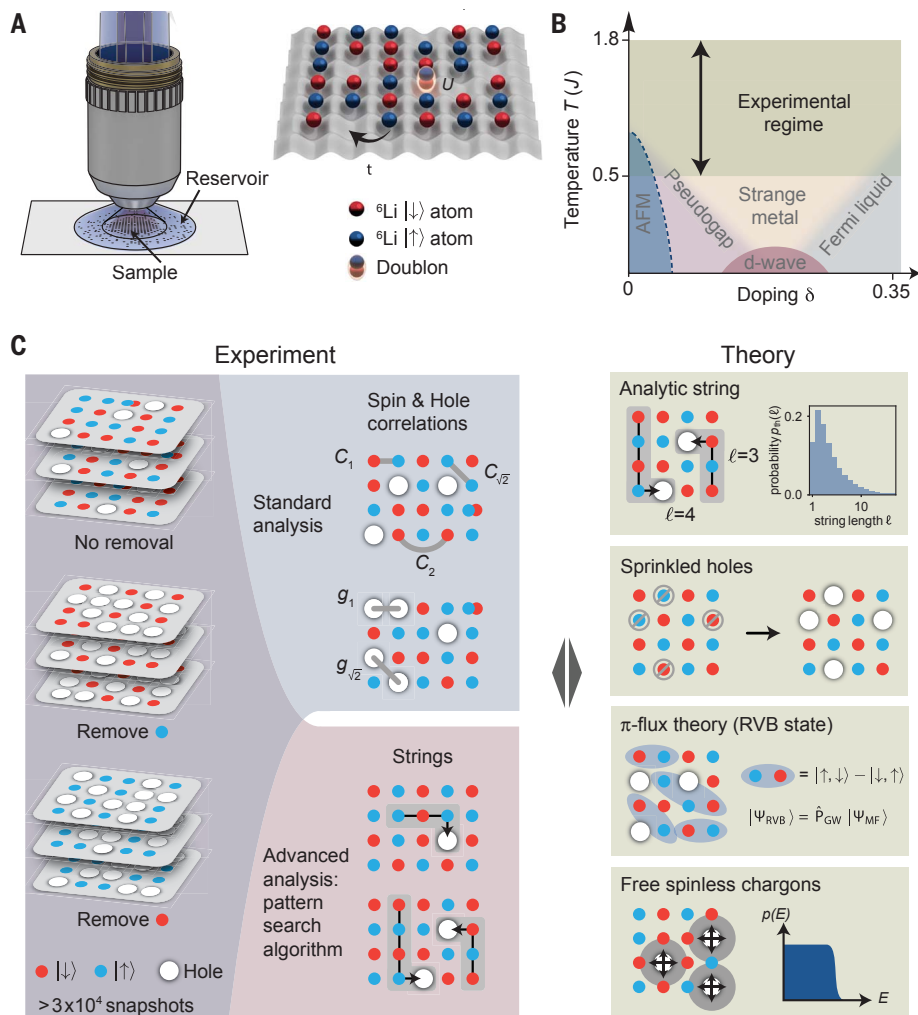


Fig. 1. Quantum simulation of the Hubbard model. (A) Quantum gases trapped in optical lattices realize the Hubbard model with tunable on-site interaction U and nearest-neighbor hopping t . Quantum gas microscopy enables site-resolved readout of the quantum state. (B) Schematic of the conjectured phase diagram of the finite-size 2D Hubbard model with the experimentally accessed regime (green shading). (C) Outline of experimental observables used and theoretical models evaluated. We evaluate theories using both standard observables and pattern-recognition-based observables using snapshots of the quantum state.

each spin along its trajectory by one lattice site, whereas the AFM quantum state remains otherwise unmodified; this is the frozen-spin approximation (20). The delocalization of each hole can then be described as a superposition state of hole trajectories, or geometric strings, whose lengths ℓ depend on the strength of AFM correlations and the ratio of the kinetic energy t to the superexchange J . For any given temperature, a distribution function $p_{\text{th}}(\ell)$ of string lengths can be obtained by sampling a Boltzmann distribution of string states (Fig. 1C).

We directly assess these microscopic theoretical approaches with a quantum gas microscope, which provides projective measurements of the quantum mechanical wave function for the doped Hubbard model in the parity-projected Fock basis. Our experimental setup consists of a balanced two-component gas of fermionic lithium in the lowest band of a square optical lattice (21), with U/t set

to 8.1(2). We selectively image one of the spin states or the total atom distribution (22). Entropy redistribution with a digital micromirror device enables a disk-shaped homogeneous system of ~ 80 sites with temperatures as low as $T/J = 0.50(4)$ (11). We alter the local chemical potential to dope the system, maintaining independent temperature control [section 7.1 of (14)]. We determine the doping from the single-particle occupation density and temperature from the nearest-neighbor spin correlator, both by comparing to numerics [section 2 of (14)].

Pattern recognition of geometric strings

We design a pattern recognition algorithm for geometric strings that we apply to real-space snapshots where doublons and one of the two spin states have been removed (Fig. 2A). Because geometric strings describe a relationship between doped and half-filled AFMs, we search for string-

like patterns in the deviation between snapshots of the doped Hubbard model and an approximation to the AFM, an exact checkerboard. For each image, we take the set of sites that deviate and extract string patterns using the following rules: (i) every string pattern is a connected subset of sites forming a path without branching points; (ii) each site can be part of only one string pattern; (iii) longer string patterns are favored; and (iv) every string pattern must have at one end a site that is detected as empty, and therefore consistent with having a hole on that site. We discuss alternate algorithms in section 3.4 of (14).

We find that this algorithm is indeed sensitive to hole doping. Figure 2B shows string-pattern length distributions $p^\delta(\ell)$ over pattern lengths ℓ , averaged over experimental data at temperatures between $0.50(4)J$ and $0.70(3)J$. As the sample is doped from half-filling to a doping δ of 10.0(8)%, the number of string patterns increases across the entire range of lengths. The appreciable distribution of string patterns $p^0(\ell)$ detected at half-filling reflects the deviation of a quantum AFM from our checkerboard approximation and therefore should be considered as a baseline level. This baseline can be reproduced through Heisenberg quantum Monte Carlo simulation [see section 3.3.3 of (14)] and is largely caused by the finite temperature and underlying SU(2) symmetry of the system. We have lessened these contributions by reducing the analysis region to a diameter of seven sites and postselecting on the staggered magnetization. In section 3.3 of (14), we show that results are robust to the choice of postselection scheme and that the limited detection of one of the spin states causes only an overall factor decrease in string patterns detected.

Next, we compare our experimental results to the simulation results of three microscopic models. We make predictions by producing artificial images and evaluating them with our string pattern detection algorithm, such that the detection is common to experiment and theoretical simulation. Beginning with the analytic string model, we generate images by randomly placing a number of holes into actual experimental images taken at half-filling, then randomly propagating each hole according to the analytically generated string-length histogram (see Fig. 1C) and appropriately displacing the spins along the hole's path. Note that this approach preserves the SU(2) symmetry of the system. The resulting string-pattern length distribution agrees with experimental data [see Fig. 2B for 10% doping], even though the theory has no free parameters.

To verify whether our measured signal simply results from the introduction of holes rather than changes to the spin background, we next compare our experimental result with simulations where holes are artificially and randomly placed ("sprinkled") into experimental data taken at half-filling, equivalent to placing one-site-long strings. The associated string-pattern length distribution $p_s^\delta(\ell)$ fails to explain the experimental results, revealing the nontrivial interplay of spin and charge degrees of freedom in the 2D doped Hubbard

model. Last, we compare our experimental result to π -flux states by fitting the nearest-neighbor spin correlator for an effective temperature and producing simulated images at 10% doping, and find quantitative agreement with experiment at short pattern lengths, but a deficit at long lengths.

We repeat the measurements for a sample heated before lattice loading to investigate temperature effects. Figure 2C shows experimental data at half-filling and at 10.1(8)% doping, along with the simulated prediction, averaged over samples at temperatures between $1.3(1)J$ and $1.8(1)J$. In contrast to colder temperatures, there is no statistically significant deviation between the experimental data with and without hole doping; $p^{0.1}(\ell) \approx p^0(\ell)$. For these temperatures, spin ordering is so weak that the resulting string patterns may mask additional effects from doping. These deviations appear to set an upper bound on the density of detectable string patterns (Fig. 2E); we therefore plot the pattern length distribution for high-temperature and half-filling as a reference for the cold temperature datasets in Fig. 2B (gray dash-dotted line).

In Fig. 2D and its inset we plot, respectively, the relative and absolute differences between the pattern-length histograms in the doped and undoped cases; these differences are shown for both the cold and hot datasets used in Fig. 2, B and C. For the undoped case, we use the sprinkled string-pattern length distribution $p_s^0(\ell)$ to account for

any deviation from the half-filling distribution resulting from the introduction of holes. Although the absolute difference does not recover the exact analytic string distribution (Fig. 1C), which can be attributed to the imperfect detection of the pattern recognition algorithm, for cold temperatures it does assume a qualitatively similar distribution. Notably, at 10.0(8)% doping we find more than three times as many length-9 patterns as there are at half filling, reflecting the large impact of holes in an AFM spin background.

Focusing on the cold dataset, we now examine the relationship between doping and the number of detected string patterns (Fig. 3A). In this string-pattern count, we omit patterns of one or two sites to avoid contributions from quantum fluctuations such as doublon-hole pairs or spin-exchange processes. The string-pattern count increases with doping and saturates at about 16% doping. This saturation is consistent with a high density of strings and overlapping or adjacent strings scrambling spin order such that pattern detection becomes insensitive to additional strings. The continued agreement between geometric strings and experiment in both the string-pattern count and the absolute difference $p^\delta(\ell) - p_s^\delta(\ell)$ suggests that the increase in number of string states is sufficient to explain the experimental data.

The experimental string-pattern count is significantly larger than that of the sprinkled-hole simulation; nonetheless, there is an increase in

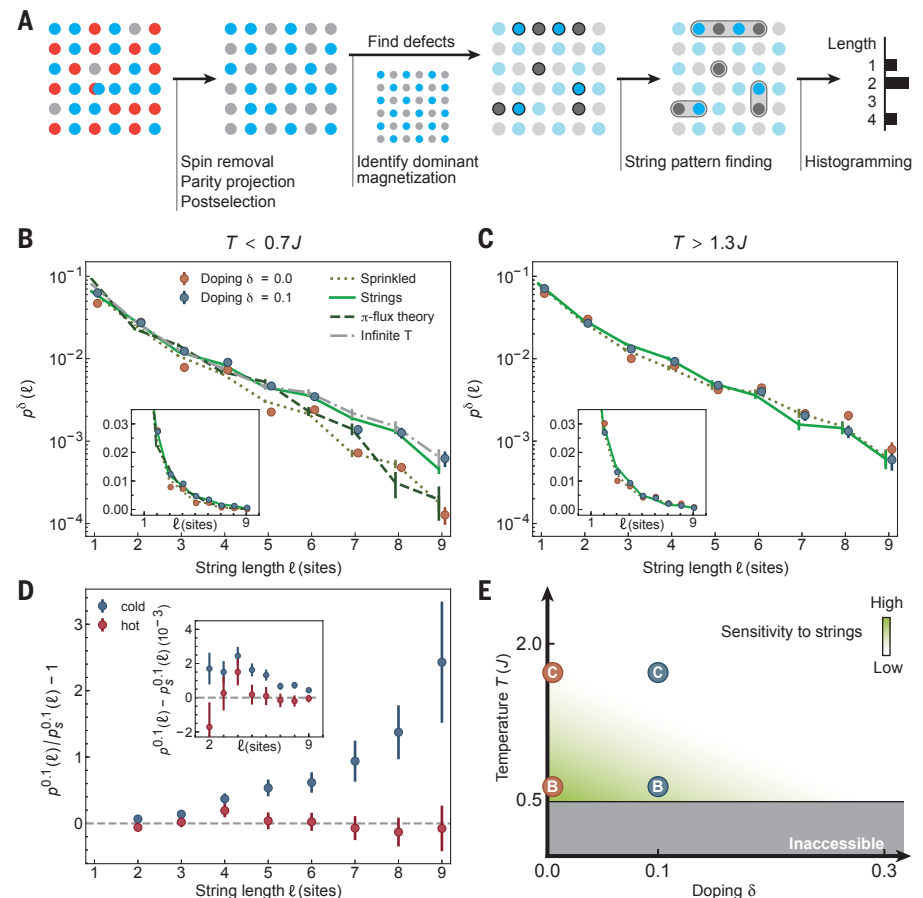
detected string patterns owing to the additional holes. The string-pattern count from π -flux states shows considerably better agreement with experimental data than with sprinkled holes, exhibiting only a slight excess of string patterns at low doping and a deficit at high doping. The largest deviations occur at low doping, which may be related to the absence of long-range order at zero temperature in π -flux states at half-filling.

The average string-pattern length quantifies the size of the region around the hole where the spin pattern is distorted by the string (Fig. 3B). The observed values are comparatively small, influenced by the large contributions from quantum fluctuations at half-filling. The average string-pattern length does not change substantially with doping, consistent with spatially isolated patterns; however, at larger dopings, we observe a slight decrease in average length that coincides with the observed saturation in the string count. This behavior is captured by the geometric-string model for low and intermediate doping. At high doping, the theory exhibits shorter average string lengths than the experiment, which may result from high-string-density effects such as string-string interactions, which are not included in the theory.

We compare these results to a dataset in which geometric strings are not expected to occur. This dataset consists of experimental images taken at various temperatures at half-filling with sprinkled holes to match each desired doping level [for

Fig. 2. Measurement of string-pattern length histograms from site-resolved snapshots.

(A) Schematic explanation of the string-pattern identification algorithm (see text). (B and C) Change in string-pattern length histograms upon doping to 10% and comparison with simulated models at 10% doping, for temperatures below (B) and above (C) the superexchange energy J . The observable is only sensitive to doping in the colder dataset, and simulated strings seem to fit the doped experimental result best. Points have been slightly offset horizontally for readability and insets plot the same data on linear-linear axes. (D) Relative and absolute (inset) difference between doped and undoped pattern-length histograms, highlighting temperature-dependent sensitivity. The sprinkled-hole result is used for the undoped case as it accounts for the change in density. (E) Regions of the phase diagram examined in (B) and (C). The string-pattern observable has sensitivity at temperatures below J and below intermediate doping. In (B), (C), and (D), histograms are normalized by the number of lattice sites analyzed and error bars represent 1 SEM from more than 5500 (half-filling, cold), 3500 (doped, cold), 2900 (half-filling, hot), and 4600 (doped, hot) images.



details, see section 3.5 of (14)]. Temperatures are chosen to match the measured staggered magnetization and capture the observed loss of AFM order. Notably, the average string-pattern length reveals that this loss through heating occurs in a fundamentally different way than through doping. For all nonzero doping, the temperature-based dataset exhibits shorter average string-pattern lengths than the experimentally measured doping dataset. As doping increases, the average length monotonically decreases. Alternatively, we match the nearest-neighbor spin correlator instead of the staggered magnetization and find an even greater distinction between the doped and temperature-based datasets.

We better understand the role of temperature in string-pattern detection by observing how the string-pattern count varies with temperature at fixed doping. For 10% doping, we plot the difference between the experiment and sprinkled-hole string-pattern counts (Fig. 3C), which are plotted separately in the inset. At our lowest temperatures, the difference is greatest. This high sensitivity is consistent with the greatest spin ordering for the parent AFM at low temperatures, accompanied by a relatively large string-pattern count from the experimental data. The difference decreases steadily with increasing temperature, predominantly owing to the increase in the sprinkled-hole string-pattern count from decreased spin ordering in the parent AFM, vanishing around $T = J$.

Spin correlations and staggered magnetization

An accurate microscopic framework for the Fermi-Hubbard model should also be able to predict more conventional observables such as two-point correlation functions, which have been used with quantum gas microscopes to quantify spin and charge order (22–25). To that end, we measure the sign-corrected spin-spin correlation function for displacements $|\mathbf{d}| = d$, averaged over all sites \mathbf{i} in the system and all experimental realizations

$$C_s(|\mathbf{d}|) \equiv (-1)^{||\mathbf{d}||} \frac{\langle \hat{S}_{\mathbf{i}}^z \hat{S}_{\mathbf{i}+\mathbf{d}}^z \rangle - \langle \hat{S}_{\mathbf{i}}^z \rangle \langle \hat{S}_{\mathbf{i}+\mathbf{d}}^z \rangle}{S^2} \quad (2)$$

where $\hat{S}_{\mathbf{i}}^z$ is the spin- S operator on site \mathbf{i} , $S = 1/2$, and $||\mathbf{d}||$ denotes the L^1 norm of \mathbf{d} , by measuring charge correlations in experimental realizations with and without spin removal (22). Thanks to the sign correction $(-1)^{||\mathbf{d}||}$, positive correlator values indicate AFM ordering. Figure 4A shows the nearest neighbor, diagonal next-nearest neighbor, and straight next-nearest neighbor spin correlators [$C_s(1)$, $C_s(\sqrt{2})$, and $C_s(2)$, respectively] as a function of doping at $T = 0.65(4)J$. At half-filling, $C_s(1)$ is substantially larger than both $C_s(\sqrt{2})$ and $C_s(2)$, owing to a strong admixture of spin singlets on adjacent sites (26). As the system is doped, all correlators exhibit a reduction in magnitude. $C_s(1)$ remains positive for all experimentally realized doping values, whereas $C_s(\sqrt{2})$ exhibits a statistically significant sign change around 20% doping. These features have been observed in experiment (22, 24, 27) and nu-

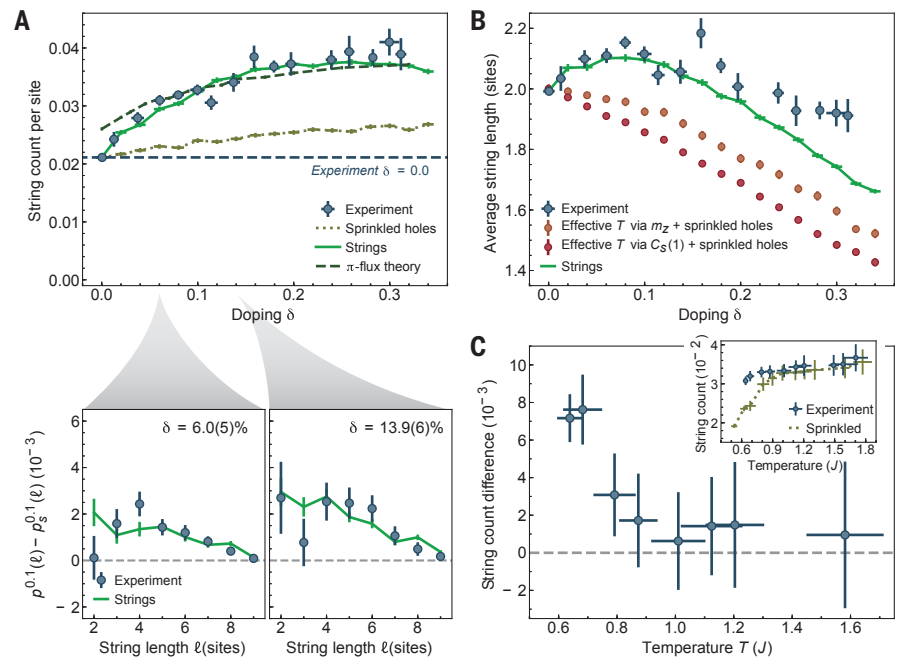


Fig. 3. Detailed examination of the detected string patterns upon doping. (A) (Top) Total number of string patterns exceeding length 2, normalized by the system size, as a function of doping. Although the string model and sprinkled-hole simulation both agree with experiment at half-filling by construction, already at low doping the string model performs significantly better than sprinkled holes. The string model is quantitatively accurate across a larger doping range than for π -flux states, but both are in greater agreement with experiment than the sprinkled-hole simulation. (Bottom) Although the absolute difference between doped and sprinkled-hole pattern-length histograms increases with doping, the shape remains roughly invariant. (B) Average string-pattern length versus doping. Doped AFMs exhibit longer-length string patterns compared to heated AFMs, even when the staggered magnetization or nearest-neighbor spin correlator is equal and holes are sprinkled in to equate doping levels (see text). (C) Total string count at 10% doping as a function of temperature, with corresponding sprinkled-hole string count subtracted. Sensitivity to strings decreases with temperature owing to decreased order in the parent AFM as seen in the sprinkled string count (inset). In (A) and (B), error bars on the doping are calculated as in (14), section 2.1. All other error bars represent 1 SEM. The figure is based on more than 24,800 experimental realizations.

merics (24), and are good benchmarks for the evaluation of theoretical models.

We make predictions for spin correlations from ensembles of non-postselected images with sprinkled holes, geometric strings, or π -flux states. By construction, at half-filling the predictions of sprinkled holes and the string model are the same as those of experimental half-filling data. Away from half-filling, sprinkled holes underestimate the decrease of the correlators because the model fails to account for the disruption of AFM order as the system is doped. By contrast, beginning at intermediate doping values, the string model overestimates the decrease of $C_s(1)$, which could stem from backaction of the background state after string-state formation. However, it explains the decrease of $C_s(\sqrt{2})$ and $C_s(2)$ on a quantitative level. The π -flux model performs well and accurately predicts $C_s(1)$ and $C_s(2)$ far from half-filling but fails to predict the sign change of $C_s(\sqrt{2})$ at intermediate doping, even when the fitted temperature is varied. The sign change of $C_s(\sqrt{2})$ is an interesting qualitative feature that is predicted and can be explained by the string model. As a direct result of spins being displaced

by one site when a string passes through, $C_s(1)$ is mixed into $C_s(\sqrt{2})$. Because $C_s(1)$ reflects opposite spin alignment from $C_s(\sqrt{2})$, this mixing results in a sign change once the contribution of $C_s(1)$ exceeds that of the original contribution strength at some critical doping.

Cold-atom experiments provide access to full-counting statistics (FCS) because of their ability to project and measure an entire quantum system at once (17). We measure the FCS of the staggered magnetization operator

$$\hat{m}^z = \frac{1}{N} \sum_{\mathbf{i}} (-1)^{||\mathbf{i}||} \hat{S}_{\mathbf{i}}^z \quad (3)$$

for system size N across all experimental realizations as we dope the system (Fig. 4B). As expected, the staggered magnetization distribution narrows, reflecting the finite-size crossover from the AFM-ordered phase (17). The sprinkled-hole simulation does not exhibit a major change in the distribution as the system is doped, as it fails to account for holes disrupting the AFM order. By contrast, both π -flux states and geometric strings demonstrate reasonable agreement with the experimentally

measured distribution function across all dopings. Across all observables considered, both of these theories perform quite well, especially in comparison to the sprinkled-holes simulation and the naïve phenomenological models detailed in section 5 of (14). However, we find the sign change of $C_s(\sqrt{2})$ to be a key qualitative feature that is captured only by geometric strings.

Antimoment correlations

All observables studied in this work thus far have focused on the spin sector of the Hubbard model. Next, we examine correlations in the charge sector. At sufficiently low temperatures, one may expect signatures of pairing (10, 28) or stripe phases (29, 30), which lead to hole bunching. However, anticorrelations of the holes, as observed previously at increased temperatures (24), are expected in the strongly correlated metallic regime of the Hubbard model. The transition between these two regimes in the Hubbard model phase diagram is not yet fully understood; however, the currently accessible experimental regime allows us to place more accurate bounds on where this transition can occur. We continue to compare experimental results to predictions of π -flux states, but do not compare to predictions of the geometric string theory because it approximates that charges are uncorrelated. Rather, because each string is associated with a single hole, correlation functions of holes can reveal possible interactions and correlations between geometric strings, should they exist.

In our experiment, doubly occupied sites appear as empty when imaged and the exact hole correlation is not directly accessible; rather, we measure “antimoment” correlations $C_h(|\mathbf{d}|)$ at a distance $|\mathbf{d}|$, which include contributions from doublon-doublon and doublon-hole correlations:

$$C_h(|\mathbf{d}|) \equiv \left(\langle (1 - \hat{n}_{s,\mathbf{i}})(1 - \hat{n}_{s,\mathbf{i}+\mathbf{d}}) \rangle - \langle (1 - \hat{n}_{s,\mathbf{i}}) \rangle \langle (1 - \hat{n}_{s,\mathbf{i}+\mathbf{d}}) \rangle \right) \quad (4)$$

where $\hat{n}_{s,\mathbf{i}}$ is the single particle occupation on site \mathbf{i} . Note that this correlator is identical to the moment correlator. At half-filling, numerics indicate positive antimoment correlations at the percent level for nearest neighbors, dominated by positive doublon-hole correlations (24). Doublon-hole pairs beyond nearest neighbors become increasingly unlikely; therefore, to avoid the effects of doublon-hole pairs, we focus on correlations at distances greater than 1. We find the nearest-neighbor antimoment correlator at half-filling to be weaker than predicted according to numerics, which may be caused by imperfect imaging fidelity. However, this effect only weakens the magnitude of the antimoment correlators measured; we therefore focus on qualitative conclusions from the experimental data.

Figure 5A shows the antimoment correlation for 3% (top) and 19% (bottom) doping at a temperature $T = 0.65(4)J$. Whereas holes appear uncorrelated close to half-filling, at larger doping qualitatively different behavior appears. We find statistically significant antimoment anticorrelations out to distances over two sites, reflecting

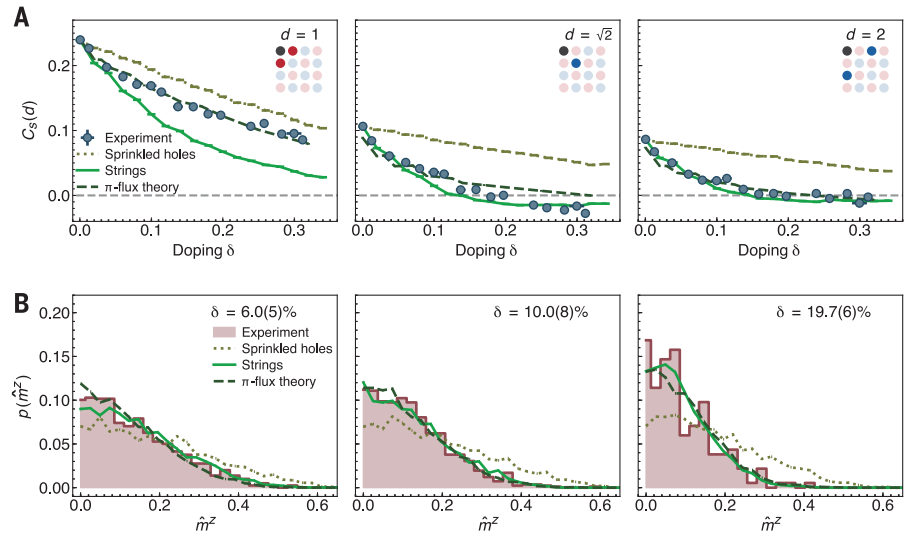


Fig. 4. Spin correlations and staggered magnetization. (A) Decay of nearest-neighbor (left), diagonal next-nearest-neighbor (center), and straight nearest-neighbor (right) spin-spin correlation functions upon doping. The π -flux theory most quantitatively explains $C_s(1)$, but only the string model captures the sign change of $C_s(\sqrt{2})$. In all three cases, sprinkled holes overestimate the spin correlations. Doping error bars are calculated as in (14), section 2.1; all other error bars represent 1 SEM. (B) Full counting statistics of the staggered magnetization for doping values of 6.0(5)% (left), 10.0(8)% (center), and 19.7(6)% (right). Both π -flux states and geometric strings show reasonable agreement, whereas sprinkled holes do not. The figure is based on more than 29,900 experimental realizations at average temperature $T = 0.65(4)J$.

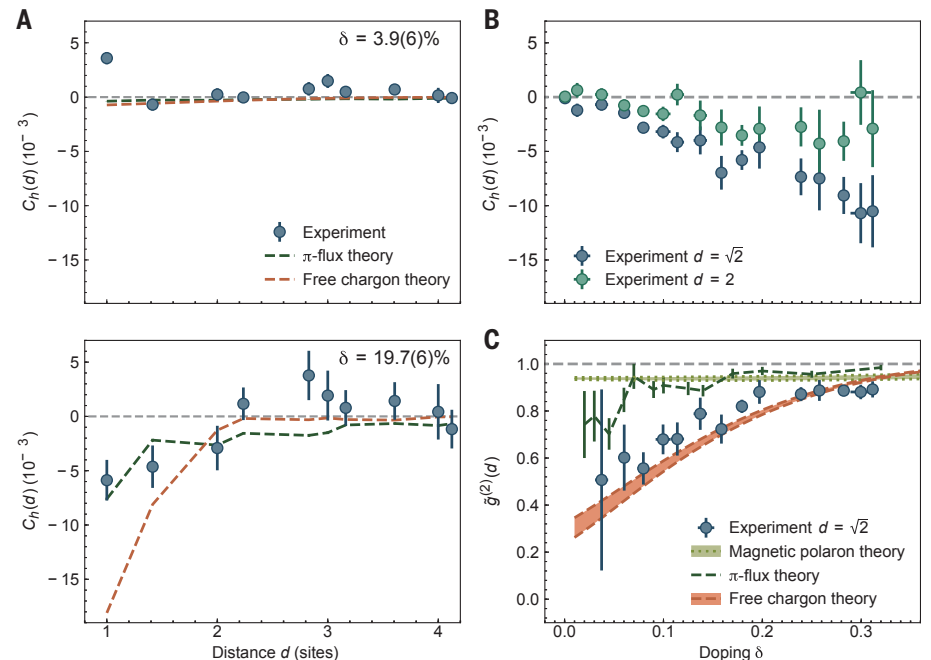


Fig. 5. Observation of hole antibunching. (A) Antimoment correlation function for weak (top) and strong (bottom) doping. The correlation functions are different up to a distance of $d = 2$. (B) Diagonal next-nearest neighbor and straight next-nearest neighbor antimoment correlators versus doping. At both distances negative correlations grow with doping. (C) Normalized antimoment correlator at $d = \sqrt{2}$ versus doping. The experimental result cannot be explained by the π -flux or a point-like magnetic polaron theory (see text), but instead matches a free fermionic chargon theory. In (B) and (C), error bars on the doping are calculated as in (14), section 2.1. All other error bars represent 1 SEM. The figure is based on more than 9900 experimental realizations at an average temperature $T = 0.65(4)J$.

hole-hole repulsion in this regime. Microscopically, such repulsive interactions can arise from the existence of a low-lying bound state of two holes (31). Here we do not consider geometric-string theory or sprinkled holes because both introduce uncorrelated holes by construction. Additionally, in the comparison to π -flux states, we do not include doublon-hole pairs to avoid unintended artifacts in the antimoment correlation. For reference, we plot the predicted hole-hole correlation function for a phenomenological model of spinless fermionic chargons with nearest-neighbor hopping of strength t and temperatures between $0.5J$ and $0.7J$ (32). Here, strong anticorrelations result from Pauli repulsion between the fermionic chargons, but qualitatively similar behavior is expected for bosonic chargons with hard-core interactions. We find that both theories qualitatively describe the experimental result.

The emergence of this repelling behavior can be characterized by plotting the antimoment correlation as a function of doping for $d = \sqrt{2}$ and $d = 2$ (Fig. 5B). Beyond the intermediate doping regime, negative correlations appear at distances of $\sqrt{2}$ and 2, suggesting a growth of hole-hole repulsion with doping. Furthermore, the presence of antimoment correlations between sites of differing sublattices at $d = 1$ evidences against holes tunneling preferentially between sites of one sublattice, as predicted by theories of pointlike magnetic polarons with a dispersion minimum at $(\pi/2, \pi/2)$ in the Brillouin zone (33–36).

Finally, we plot a normalized $g^{(2)}(d = \sqrt{2})$ to account for the difference between doped holes and holes in doublon-hole pairs and quantify the relative fraction of doped holes that are anticorrelated:

$$\tilde{g}^{(2)}(|\mathbf{d}|) \equiv \frac{C_h(\mathbf{d})}{\delta^2} + 1 \quad (5)$$

for doping δ (Fig. 5C). This rescaling allows direct comparison to the $g^{(2)}$ function for theories without doublon-hole pairs. The number of free holes is too small for doping below 5% to make statistically significant statements about the behavior of holes in this regime. In the geometric-string theory, we assume that chargons (dressed dopants) are completely uncorrelated with each other, but because of their fermionic statistics, Pauli blocking should actually introduce anticorrelations that have not yet been included in our analyses. We first consider a description of these chargons as pointlike magnetic polarons, where the known dispersion relation of the dressed hole (37) is used to define a tight-binding hopping model of the polaron. Figure 5C shows that our data are incompatible with this model, which predicts significantly weaker hole-hole anticorrelations. Similar behavior is predicted by the π -flux theory, which models the doped holes as pointlike objects moving in a quantum spin liquid of singlets.

Next, we examine a picture of free chargons, motivated by considering magnetic polarons with a finite extent that results from the spinon-charge bound state predicted by geometric-

string theory. At sufficiently large charge density, or doping, the chargons are expected to interact, and their hard-core character will introduce anticorrelations. In this regime, geometric strings are also expected to overlap substantially and modify the dispersion relation of the chargons to be independent of spinons, yielding spinless chargons. We find that the experimental results demonstrate consistency with these free chargons, in agreement with earlier theoretical work in the strange-metal regime (32, 38). This extension to the geometric string theory may be able to explain the deviations from experiment seen in other observables at high doping, but additional analyses are required.

Conclusions and outlook

The string-pattern-based observables introduced here complement established observables such as correlation functions or full counting statistics. Across the observables considered, we find better agreement with experimental data between both the geometric-string theory and π -flux states, as compared to sprinkled holes.

At intermediate doping values, we find evidence for hole-hole repulsion. Although signatures of other phases such as stripe phases, incommensurate spin order, or nematic fluctuations have not yet been observed in this system, they are predicted to emerge at lower temperatures.

The ideas presented can be extended to other real-space patterns—for example, patterns that reflect the underlying physics of other candidate microscopic theories for the doped Hubbard model. Moreover, machine learning techniques could be used to directly compare sets of raw experimental atom distributions to theoretical models without the need for intermediate observables (39). This class of techniques is highly promising as quantum simulations of the Hubbard model continue to probe lower temperatures within the pseudogap and strange-metal phases, but can also be applied to spatially resolved studies of quenches across phase transitions (40), dynamical phase transitions (41), and higher-order scattering processes (42). Possible extensions of our work include systems with anisotropic spin interactions (16) or doped $SU(N)$ spin models (43).

REFERENCES AND NOTES

1. E. H. Lieb, F. Y. Wu, *Phys. Rev. Lett.* **20**, 1445–1448 (1968).
2. F. Woynarovich, *J. Phys. Chem.* **15**, 85–96 (1982).
3. M. Ogata, H. Shiba, *Phys. Rev. B Condens. Matter* **41**, 2326–2338 (1990).
4. H. V. Kruijs, I. P. McCulloch, Z. Nussinov, J. Zaanen, *Phys. Rev. B* **70**, 075109 (2004).
5. M. Endres *et al.*, *Science* **334**, 200–203 (2011).
6. C. Gross, I. Bloch, *Science* **357**, 995–1001 (2017).
7. T. A. Hilker *et al.*, *Science* **357**, 484–487 (2017).
8. V. J. Emery, *Phys. Rev. Lett.* **58**, 2794–2797 (1987).
9. P. A. Lee, N. Nagaosa, X.-G. Wen, *Rev. Mod. Phys.* **78**, 17–85 (2006).
10. B. Keimer, S. A. Kivelson, M. R. Norman, S. Uchida, J. Zaanen, *Nature* **518**, 179–186 (2015).
11. A. Mazurenko *et al.*, *Nature* **545**, 462–466 (2017).
12. P. W. Anderson, *Science* **235**, 1196–1198 (1987).
13. X.-G. Wen, P. A. Lee, *Phys. Rev. Lett.* **76**, 503–506 (1996).
14. See supplementary materials.
15. C. Gros, *Ann. Phys.* **189**, 53–88 (1989).
16. F. Grusdt *et al.*, *Phys. Rev. X* **8**, 011046 (2018).

17. L. N. Bulavaevskii, É. L. Nagaev, D. I. Khomskii, *J. Exp. Theor. Phys.* **27**, 836–838 (1968).
18. W. F. Brinkman, T. M. Rice, *Phys. Rev. B* **2**, 1324–1338 (1970).
19. P. Béran, D. Poilblanc, R. B. Laughlin, *Nucl. Phys. B* **473**, 707–720 (1996).
20. F. Grusdt, Z. Zhu, T. Shi, E. Demler, *SciPost Physics* **5**, 057 (2018).
21. M. F. Parsons *et al.*, *Phys. Rev. Lett.* **114**, 213002 (2015).
22. M. F. Parsons *et al.*, *Science* **353**, 1253–1256 (2016).
23. M. Boll *et al.*, *Science* **353**, 1257–1260 (2016).
24. L. W. Cheuk *et al.*, *Science* **353**, 1260–1264 (2016).
25. P. T. Brown *et al.*, *Science* **357**, 1385–1388 (2017).
26. E. V. Gorelik *et al.*, *Phys. Rev. A* **85**, 061602 (2012).
27. J. Koepsell *et al.*, Imaging magnetic polarons in the doped Fermi-Hubbard model. arXiv:1811.06907 [cond-mat.quant-gas] (2018).
28. V. J. Emery, S. A. Kivelson, *Nature* **374**, 434–437 (1995).
29. S. R. White, D. J. Scalapino, *Phys. Rev. Lett.* **80**, 1272–1275 (1998).
30. J. Zaanen, O. Y. Osman, H. V. Kruijs, Z. Nussinov, J. Tworzydło, *Philos. Mag. B Phys. Condens. Matter Stat. Mech. Electron. Opt. Magn. Prop.* **81**, 1485–1531 (2001).
31. C. Chin, R. Grimm, P. S. Julienne, E. Tiesinga, *Rev. Mod. Phys.* **82**, 1225–1286 (2010).
32. R. K. Kaul, Y. B. Kim, S. Sachdev, T. Senthil, *Nat. Phys.* **4**, 28–31 (2007).
33. C. L. Kane, P. A. Lee, N. Read, *Phys. Rev. B Condens. Matter* **39**, 6880–6897 (1989).
34. S. Sachdev, *Phys. Rev. B Condens. Matter* **39**, 12232–12247 (1989).
35. G. Martínez, P. Horsch, *Phys. Rev. B Condens. Matter* **44**, 317–331 (1991).
36. J. Liu, X. Sun, D. L. Lin, T. F. Georgy, *J. Phys. Condens. Matter* **4**, 5301–5308 (1992).
37. M. Brunner, F. F. Assaad, A. Muramatsu, *Phys. Rev. B* **62**, 15480–15492 (2000).
38. S. Sachdev, D. Chowdhury, *Prog. Theor. Exp. Phys.* **2016**, 12C102 (2016).
39. A. Bohrdt *et al.*, *Nat. Phys.* (2019).
40. H. Bernien *et al.*, *Nature* **551**, 579–584 (2017).
41. J. Zhang *et al.*, *Nature* **551**, 601–604 (2017).
42. L. Feng, J. Hu, L. W. Clark, C. Chin, *Science* **363**, 521–524 (2019).
43. C. Honerkamp, W. Hofstetter, *Phys. Rev. Lett.* **92**, 170403 (2004).
44. C. S. Chiu *et al.*, Data for “String patterns in the doped Hubbard model.” Harvard Dataverse (2019).

ACKNOWLEDGMENTS

We thank M. Kanász-Nagy for Heisenberg QMC code. We thank A. Hébert, S. Sachdev, Z.-Y. Weng, and J. Zaanen for insightful discussions. **Funding:** We acknowledge support from AFOSR grant nos. FA9550-14-1-0035 and FA9550-16-1-0323; DoD NDSEG; the Gordon and Betty Moore Foundation EPIQS program and grant no. 6791; NSF GRFP and grant nos. PHY-1506203, PHY-1734011, and DMR-1308435; ONR grant no. N00014-18-1-2863; SNSF; Studienstiftung des deutschen Volkes; and the Technical University of Munich–Institute for Advanced Study, funded by the German Excellence Initiative and the European Union FP7 under grant agreement 291763, the Deutsche Forschungsgemeinschaft (DFG, German Research Foundation) under Germany’s Excellence Strategy–EXC-2111–390814868, through DFG grant no. KNI254/1-1, and DFG TRR80 (Project F8). **Author contributions:** C.S.C., G.J., M.X., and D.G. performed the experiment. C.S.C. and A.B. curated the data and, along with F.G., developed the pattern finding algorithm. C.S.C., G.J., A.B., M.X., and D.G. analyzed the data. F.G. and E.D. developed the geometric-string theory. A.B. and F.G., together with M.K. and E.D., developed the theory simulations. M.G. and D.G. supervised the work. All authors contributed to the interpretation of the results and writing of the manuscript.

Competing interests: The authors declare no competing interests.

Data and materials availability: All experimentally measured site-resolved atom distributions and analysis code are available (44).

SUPPLEMENTARY MATERIALS

science.sciencemag.org/content/365/6450/251/suppl/DC1
Supplementary Text
Figs. S1 to S10
References (45–57)

26 September 2018; accepted 5 June 2019
10.1126/science.aav3587

String patterns in the doped Hubbard model

Christie S. Chiu, Geoffrey Ji, Annabelle Bohrdt, Muqing Xu, Michael Knap, Eugene Demler, Fabian Grusdt, Markus Greiner and Daniel Greif

Science **365** (6450), 251-256.
DOI: 10.1126/science.aav3587

Looking for patterns in an optical lattice

One of the simplest models of interacting fermions on a two-dimensional (2D) lattice—the Hubbard model—becomes too tricky to simulate on classical computers as the density of empty lattice sites (holes) increases. Chiu *et al.* used a quantum microscope to take snapshots of thousands of realizations of the 2D Hubbard model in an optical lattice filled with fermionic lithium atoms at varying hole densities (see the Perspective by Schauss). The authors used pattern recognition algorithms to analyze the images, in which each lattice site was individually resolved. Comparing these patterns to the predictions of several theoretical models, they found the most consistency with the so-called geometric string model.

Science, this issue p. 251; see also p. 218

ARTICLE TOOLS

<http://science.sciencemag.org/content/365/6450/251>

SUPPLEMENTARY MATERIALS

<http://science.sciencemag.org/content/suppl/2019/07/17/365.6450.251.DC1>

RELATED CONTENT

<http://science.sciencemag.org/content/sci/365/6450/218.full>

REFERENCES

This article cites 56 articles, 12 of which you can access for free
<http://science.sciencemag.org/content/365/6450/251#BIBL>

PERMISSIONS

<http://www.sciencemag.org/help/reprints-and-permissions>

Use of this article is subject to the [Terms of Service](#)

Science (print ISSN 0036-8075; online ISSN 1095-9203) is published by the American Association for the Advancement of Science, 1200 New York Avenue NW, Washington, DC 20005. The title *Science* is a registered trademark of AAAS.

Copyright © 2019 The Authors, some rights reserved; exclusive licensee American Association for the Advancement of Science. No claim to original U.S. Government Works